REVISION 1

Word Count: 3275 words

Atomic-scale interlayer friction of gibbsite is lower than brucite due to interactions of hydroxyls

Hanaya Okuda,[1,2,*] Kenji Kawai,[1] Hiroshi Sakuma[3]

[1] Department of Earth and Planetary Science, School of Science, University of Tokyo, Bunkyo, Tokyo 113-0033, Japan

[2] Department of Ocean Floor Geoscience, Atmosphere and Ocean Research Institute, University of Tokyo, Kashiwa, Chiba 277-8564, Japan

[3] Functional Clay Materials Group, National Institute for Materials Science, Tsukuba, Ibaraki 305-0044, Japan

[*] Corresponding Author: Hanaya Okuda, Department of Ocean Floor Geoscience, Atmosphere and Ocean Research Institute, University of Tokyo, 5-1-5 Kashiwanoha, Kashiwa, Chiba 277-8564, Japan. (okuda@aori.u-tokyo.ac.jp)

Abstract

To investigate the role of atomic-scale structure on frictional properties of gibbsite, a dioctahedral-type aluminum hydroxide, we calculated the atomic-scale interlayer shear properties using the first-principles method based on density functional theory. We found that the presence of vacant sites within the octahedral sheet of gibbsite enables hydroxyls to move to more stable positions and reduce the repulsive force, leading to a lower atomic-scale shear stress of gibbsite compared with brucite, a trioctahedral-type magnesium hydroxide. We also estimated the macroscopic single-crystal friction coefficient of gibbsite with the assumption that only the atomic-scale interlayer friction controls macroscopic friction. The estimated single-crystal friction coefficient for gibbsite is 0.36(6), which is clearly lower than the experimentally obtained friction coefficient of the powdered gouge of gibbsite (0.74). This difference between the interlayer friction coefficient and gouge friction coefficient suggests the presence of mechanisms that affect the frictional strength, such as microstructures within a fault gouge.

Keywords

Layered structure minerals, Interlayer friction, Gouge friction, Gibbsite

Introduction

Frictional strength is a fundamental physical property that controls the localization of deformation within a fault zone. Layered structure minerals have lower friction coefficients than common rock-forming minerals (Byerlee 1978; Morrow et al. 2000; Moore and Lockner 2004). The presence of layered structure minerals can creep the San Andreas fault (Carpenter et al. 2011; Lockner et al. 2011), activate low angle normal faults (Viti and Collettini 2009; Collettini et al. 2019), and reduce frictional strengths of plate boundaries in subduction zones (Ikari et al. 2018; Okuda et al. 2021b). The low friction coefficients of layered structure minerals have been explained by their characteristic crystal structure (Morrow et al. 2000; Moore and Lockner 2004; Behnsen and Faulkner 2012; Kawai et al. 2015; Sakuma and Suehara 2015; Niemeijer 2018; Okamoto et al. 2019; den Hartog et al. 2020). The frictional strength between the layers of layered structure minerals critically affects the low friction coefficients of these minerals as demonstrated by friction experiments of single-crystal phyllosilicates (Kawai et al. 2015; Niemeijer 2018; Okamoto et al. 2019). Based on the importance of interlayer shear sliding properties, we recently focused on the atomic-scale interlayer interactions and quantitatively evaluated its influence of interlayer sliding on macroscopic frictional properties (Sakuma et al. 2018, 2020, 2022;

52 Okuda et al. 2019). These studies are hereinafter referred to as SKKS18, SKK20, SLSD22,
53 and OKS19, respectively. In SKKS18, the estimated macroscopic friction coefficient of
54 muscovite was found to be nearly identical to the experimentally obtained friction
55 coefficient of single-crystal muscovite. OKS19 and SKK20 estimated slightly higher and
56 lower single-crystal friction coefficients for brucite and pyrophyllite, respectively,
57 compared with that for muscovite. SLSD22 found that the friction coefficients for
58 interlayer sliding of montmorillonite positively depend on the ionic radii of interlayer
59 cations. These studies suggested that the difference in frictional properties for the interlayer
60 sliding potentially plays a role in the difference in macroscopic friction coefficients of
61 layered structure minerals.
62 In this study, we simulated the single-crystal friction coefficient of gibbsite using the
63 density functional theory. Gibbsite ($Al(OH)_3$) has a similar crystal structure as that of
64 brucite ($Mg(OH)_2$), which was studied in OKS19. Experimentally obtained friction
65 coefficients of the gouges of gibbsite and brucite were quite different; the value for gibbsite
66 is 0.74, whereas that for brucite is 0.39 (Moore and Lockner 2004; Okuda et al. 2021a). To
67 evaluate their interlayer frictional properties and their roles in their single-crystal and gouge
68 friction coefficients, herein, we discuss the difference in friction coefficients of gibbsite and

brucite and other layered structure minerals based on theoretical consideration of the atomic-scale shear deformation.

Materials

$Al(OH)_3$ gibbsite is a dioctahedral-type layered structure mineral (Figure 1a). The space group is $P2_1/n$ with lattice constants of a = 8.684(1) Å, b = 5.078(1) Å, c = 9.736(2) Å, and β = 94.54(1)° under an ambient pressure condition (Saalfeld and Wedde 1974). The primitive unit cell of gibbsite contains two sheets of Al octahedra. Half of the hydroxyls on the dioctahedral sheet lie parallel to the sheet and the rest stand normal to the sheet because one-third of the cation sites within the gibbsite sheet are vacant (Figure 1a). In contrast to gibbsite, $Mg(OH)_2$ brucite has no vacant site, and hence, all the hydroxyls stand normal to the sheet (Figure 1b).

Methods

Potential energy surface and atomic-scale friction

The atomic-scale friction can be calculated by the required force to climb the peak of potential energy under a given normal stress condition (Zhong and Tománek 1990;

This is the peer-reviewed, final accepted version for American Mineralogist, published by the Mineralogical Society of America.
The published version is subject to change. Cite as Authors (Year) Title. American Mineralogist, in press.
DOI: https://doi.org/10.2138/am-2022-8561. http://www.minsocam.org/

Tománek et al. 1991). In this study, we referred to previous studies of SKKS18, OKS19, SKK20, and SLSD22 for the method to calculate the potential energy. We prepared a supercell that includes two Al-dioctahedral sheets and computed the interlayer energy $E_{ad}(\boldsymbol{x},z)$ at various displacements $\boldsymbol{x}$ of top sheet in the *ab* plane (~0.3 Å-mesh grid) and various interlayer distances z (0.05 Å interval; Figure 2a). This study only focuses on two layers adjacent to the shear plane because the difference in the shear stress between two and four-layers simulations is less than 1.2% for brucite (Okuda et al. 2019). Here, $E_{ad}(\boldsymbol{x},z)$ is defined as:

$$E_{\mathrm{ad}}(\boldsymbol{x},z) = E_{\mathrm{total}}(\boldsymbol{x},z) - E_{\mathrm{lower}} - E_{\mathrm{upper}}, \#(1)$$

where $E_{total}(\boldsymbol{x},z)$, E_{lower}, and E_{upper} are the calculated energies after the relaxation of positions of atoms for the supercell containing two layers, only the lower layer, and the upper layer, respectively. During the structural relaxation, the positions of Al atoms were fixed to define the positions of upper and lower layers. When a normal force f_n is applied, the interlayer distance z indicates the position where f_n balances with the repulsive interlayer force. The interlayer distance z under the normal force f_n is calculated as the distance satisfying the following relation (Figure 2b):

This is the peer-reviewed, final accepted version for American Mineralogist, published by the Mineralogical Society of America.
The published version is subject to change. Cite as Authors (Year) Title. American Mineralogist, in press.
DOI: https://doi.org/10.2138/am-2022-8561. http://www.minsocam.org/

$$f_{\mathrm{n}} = -\frac{\partial}{\partial z} E_{\mathrm{ad}}(\boldsymbol{x}, z). \#(2)$$

The normal stress σ_{n} is defined as $\sigma_{\mathrm{n}} = f_{\mathrm{n}} / S$ where S is the basal area of the supercell (Figure 2a). The potential energy $V(\boldsymbol{x},f_{\mathrm{n}})$ was then calculated by summing the interlayer energy and the required work to move layers vertically against the applied normal force, as follows:

$$V(\boldsymbol{x}, f_{\mathrm{n}}) = E_{\mathrm{ad}}(\boldsymbol{x}, z) + f_{\mathrm{n}} z. \#(3)$$

The potential energy as a function of the displacement of top layer $\boldsymbol{x}$ in the *ab* plane (equation 3) is referred to as the potential energy surface (PES, Figure 3a). The shear force $f_{\mathrm{s}}(\boldsymbol{x}, f_{\mathrm{n}})$ at the displacement $\boldsymbol{x}$ of upper layer along a given sliding path and under the applied normal force f_{n} is obtained from the derivative of the potential energy along the sliding path (Figure 3b):

$$f_{\mathrm{s}}(\boldsymbol{x}, f_{\mathrm{n}}) = \frac{\partial}{\partial \boldsymbol{x}} V(\boldsymbol{x}, f_{\mathrm{n}}). \#(4)$$

Note that we interpolated $V(\boldsymbol{x}, f_{\mathrm{n}})$ on grid points by the radial basis function with multiquadric function ($\phi(r)=(1+(\varepsilon r)^2)^{1/2}$ where r is the norm from the coordinate of a grid point, and ε is the adjustable constant) to obtain a smooth PES. The shear force along a sliding path can be categorized to two parts, namely the energy conservative part where $f_{\mathrm{s}}(\boldsymbol{x},f_{\mathrm{n}})>0$ and the energy nonconservative part where $f_{\mathrm{s}}(\boldsymbol{x},f_{\mathrm{n}})<0$ (Figure 3b). Because the

116 energy nonconservative part of sliding is assumed not to contribute to friction (Zhong and
117 Tománek 1990; Tománek et al. 1991), the averaged friction force f_{ave} on a given sliding
118 path is defined as:

$$f_{\mathrm{ave}} = \frac{1}{L}\int_0^L f_{\mathrm{f}}(\boldsymbol{x}, f_{\mathrm{n}})d\boldsymbol{x} = \frac{1}{L}\sum_{j=1}^{N} \Delta PE_j \,, \#(5)$$

119 where N is the total number of conservative parts within a given sliding path, ΔPE_j is the
120 accumulated potential energy at the j-th conservative part of sliding (see Figure 3a), L is the
121 total shear displacement on the given sliding path, and the friction force contributed only by
122 the energy conservative part $f_f(\boldsymbol{x},f_n)$ in equation 5 is defined as:

$$f_{\mathrm{f}}(\boldsymbol{x}, f_{\mathrm{n}}) = \begin{cases} f_{\mathrm{s}}(\boldsymbol{x}, f_{\mathrm{n}}) \ (f_{\mathrm{s}} \geq 0) \\ 0 \ (f_{\mathrm{s}} < 0) \end{cases} . \#(6)$$

123 We examined the shear direction dependence by computing 360 linear sliding paths by
124 changing the direction by 1° from the [1 0 0] direction.
125
126 **Density functional theory calculations**
127 The potential energies were computed using the first-principles method based on density
128 functional theory (DFT). Quantum ESPRESSO (Giannozzi et al. 2009), was used for all the
129 computations. The exchange-correlation energy was expressed using the generalized

gradient approximation with Perdew-Burke-Ernzerhof correlation functional (Perdew et al. 1996). The van der Waals interaction was corrected by using the DFT-D2 method (Grimme 2006). Only valence electrons were considered using the GBRV pseudopotential method (Garrity et al. 2014). Cutoff energies of 40.0 Ry and 320.0 Ry were applied for wave functions and for electron density, respectively. K-points of 6×6×4 were selected (Monkhorst and Pack 1976), and convergence thresholds of 0.01 mRy and 0.1 mRy/Bohr were applied for the total energy changes and the all components of all forces, respectively. We set the initial lattice parameters to a = 8.684 Å, b = 5.078 Å, c = 9.736 Å, and β = 94.54° (Saalfeld and Wedde 1974) for the most stable lattice constants (bulk structure) of gibbsite. The supercell for the calculations of the PES is a = 8.673 Å, b = 5.054 Å, c = 28.547 Å (including vacuum space), and β = 93.34° based on the obtained bulk structure.

Results and Discussion

Bulk structure of gibbsite

The calculated lattice parameters of gibbsite are a = 8.673 Å, b = 5.054 Å, c = 9.516 Å, and β = 93.34°, which are consistent with previously reported lattice parameters of gibbsite at ambient pressure condition (Table S1). We also calculated the lattice parameters under

147 hydrostatic compression of up to 3 GPa and the compression curve is consistent with the
148 results reported in previous studies (Table S2, Figure S1). Therefore, the applied
149 computational conditions would appropriately simulate the atomic-scale deformation of
150 gibbsite because the calculation reproduces the interatomic interactions from ambient
151 pressure to high pressure.
152
153 **Potential energy change by interlayer sliding (Potential energy surface, PES)**
154 The calculated PESs for gibbsite and brucite are shown in Figure 4. The potential energies
155 for brucite were calculated in our previous study (Okuda et al. 2019).
156 For gibbsite, the lowest and highest potential energies were observed at the position of top
157 layer at (e) and (f) in Figure 4c, respectively. The variations in the potential energy are
158 explained by the repulsion among the hydroxyls of the upper and lower layers. At the
159 position (f) in Figure 4c, the hydroxyls of the upper layer are located just above those of the
160 lower layer (Figure 4f), resulting in high repulsion and unstable high potential energy. At
161 the position (e) in Figure 4c, the distance among hydroxyls on both layers is large (Figure
162 4e), and hence, the lowest potential energy was achieved. Other high potential energies on
163 the PES for gibbsite are also explained by short distance among the hydroxyls of the upper

and lower layers.

For brucite, the lowest and highest potential energies were observed at the positions of top layer at (g) and (h) in Figure 4d, respectively. The reason for the variations is the same as that for gibbsite: the hydroxyls on both the upper and lower layers face each other in the unstable stacking at (h) in Figure 4d (Figure 4h for its crystal structure), whereas the hydroxyls do not face each other in the stable stacking at (g) in Figure 4d (Figure 4g for its crystal structure).

Based on relations between potential energy and stacking structures observed in both gibbsite and brucite, we conclude that energy instability during deformation is primarily controlled by configuration of hydroxyls on both layers. At some locations (e.g., sliding from (i) to (j) in Figure 4c with a sliding distance of ~0.3 Å, Figures 4i and 4j for their crystal structures), the angles of the hydroxyls on gibbsite layers changed from normal to parallel to the surface or vice versa to achieve a more stable crystal structure during deformation. This change in the angle of hydroxyls can occur because of the presence of vacant sites in the dioctahedral sheet. In contrast, brucite does not have any vacant site in the trioctahedral sheet and the angle of hydroxyls is almost fixed during the deformation.

Atomic-scale shear stress: dependence on normal stress

We calculated the atomic-scale shear stress $\tau_{atom} = f_{ave} / S$ from the obtained PES as a function of normal stresses (Figure 5a). The shear stress was calculated by averaging the shear stresses of 360 linear sliding paths of different sliding directions (Figure 5b). The error bars represent the standard deviations. The average shear stress of gibbsite is lower than brucite at all normal stresses from 0 to 5 GPa. The difference in the shear stress between gibbsite and brucite can be interpreted by the difference in the repulsion of the hydroxyls. The lying hydroxyls of gibbsite prevent the hydroxyls on both the upper and lower layers from approaching close to each other compared with those of brucite. Therefore, the potential energy during deformation does not increase easily in gibbsite compared with brucite under a given normal stress condition.

The gradient of the shear stress to the normal stress of gibbsite is smaller than that of brucite (Figure 5a). This could also be due to the stability of the hydroxyls of gibbsite. As the normal stress increases, the distance between the upper and lower layers decreases (Figure 2b). Hence, the hydroxyls on both layers also approach close to each other, increasing the potential energy and shear stress. For gibbsite, however, the presence of vacant sites enables hydroxyls to move to a more stable position, and hence, the distance

198 between hydroxyls would not easily decrease. Conversely, brucite does not have vacant
199 sites within its layer; therefore, the distance between hydroxyls effectively decreases as the
200 interlayer distance decreases, which increases the potential energy and shear stress.
201
202 **Atomic-scale shear stress: dependence on sliding directions**
203 For brucite (Okuda et al. 2019), the atomic-scale shear stress τ_{atom} exhibited little sliding
204 direction dependence (gray line in Figure 5b). For gibbsite, a clear sliding direction
205 dependence was observed. The directions around [0 1 0] (90°) yielded a high τ_{atom} of 0.8
206 GPa, whereas the directions around [1 0 0] (0°) yielded a low τ_{atom} of 0.5 GPa at a normal
207 stress of 2.5 GPa (black line in Figure 5b). The difference in the shear stress would be due
208 to the presence of high potential energy area around at (f) in Figure 4c. As this high
209 potential area elongates parallel to [1 0 0], the gradient to climb the potential ridge is
210 changed by the sliding direction. For instance, we consider two sliding paths, [2 1 0] and [1
211 3 0], that cross the potential ridge shown as white area with different angles (Figure 6a)
212 having the same L value of 18 Å. Path [2 1 0] crossed the potential ridge with a low angle,
213 whereas path [1 3 0] crossed the potential ridge with a high angle (Figure 6a). Although the
214 maximum heights of the potential are similar (1.4 eV for [2 1 0] and 1.7 eV for [1 3 0] at a

normal stress of 2.5 GPa, Figure 6b), the cumulative potential energy during the conservative part of sliding along path [1 3 0] is higher than that along path [2 1 0] (Figure 6c). This is caused by the higher gradient to climb the potential ridge (i.e., shear stress) along path [1 3 0] than along path [2 1 0] (hatched area in Figure 6d). Consequently, path [1 3 0] had a high τ_{atom} of 0.76 GPa and path [2 1 0] had a low τ_{atom} of 0.50 GPa because the high cumulative potential energy contributes directly to high shear stress according to equation 5. As presented above, the direction dependence of gibbsite is influenced by the angle that crosses the potential ridge: when the sliding path is subparallel to [1 0 0] (0°), the angle becomes small, which leads to a low shear stress, whereas when the sliding path is subparallel to [0 1 0] (90°), the angle becomes high leading to a high shear stress. In contrast, the potential ridge at (h) in Figure 4d for brucite is isotropic, which makes little variation in shear stress to climb the potential ridge from any sliding direction. Hence, knowing the PES is critically important to elucidate the atomic-scale frictional properties of layered structure minerals as the difference in atomic-scale frictional characteristics between gibbsite and brucite is originated from the difference in the shape of potential ridge.

Implications for Macroscopic Friction Coefficients of Gibbsite and Brucite

This is the peer-reviewed, final accepted version for American Mineralogist, published by the Mineralogical Society of America.
The published version is subject to change. Cite as Authors (Year) Title. American Mineralogist, in press.
DOI: https://doi.org/10.2138/am-2022-8561. http://www.minsocam.org/

Interlayer macroscopic friction coefficient

In the previous sections, we discussed the atomic-scale interlayer friction of gibbsite and brucite and demonstrated that gibbsite has a lower atomic-scale shear stress than brucite. In this section, we discuss the interlayer macroscopic friction coefficients of layered structure minerals. The interlayer macroscopic friction coefficient μ_M can be calculated using two deformation properties at the asperity contact: the shear stress at the asperity contact τ and the yield strength of the material p, as follows (Bowden and Tabor 1950):

$$\mu_M = \frac{\tau}{p}. \#(7)$$

Assuming that the theoretically calculated atomic-scale interlayer friction τ_{atom} is τ and the experimental indentation hardness is p, equation 7 results in a nearly identical value to the experimentally measured macroscopic friction coefficient in the case of single crystal muscovite (Sakuma et al. 2018). Based on the yield strength p for gibbsite of 1.8(2) GPa (Wijayaratne et al. 2017) and the calculated atomic-scale shear stress of τ_{atom} = 0.65(9) GPa at a normal stress of 1.8 GPa, the μ_M value was estimated to be 0.36(6). Both $\tau_{atom}(p)$ and p for gibbsite were lower than those of brucite (Wijayaratne et al. 2017; Okuda et al. 2019), whereas the estimated μ_M for gibbsite of 0.36(6) was higher than that for brucite of 0.31(3) (Table 1).

248

249 **Application to gouge friction coefficient**

250 Since the estimated μ_M for gibbsite was higher than that for brucite, the difference in the
251 experimentally obtained gouge friction coefficient μ_g between two minerals (0.74 for
252 gibbsite, 0.39 for brucite, Table 1) would be partially contributed by the difference in μ_M.
253 However, an additional frictional mechanism will be required to fully explain the difference
254 in μ_g. Most interlayer macroscopic frictions μ_M are lower than the gouge friction μ_g as
255 reported for brucite (Okuda et al. 2019, 2021a), pyrophyllite (Moore and Lockner 2004;
256 Sakuma et al. 2020), muscovite (Kawai et al. 2015; Sakuma et al. 2018), and
257 montmorillonite (Sakuma et al. 2022). Mohs hardness may be related to μ_g (Moore and
258 Lockner 2004), although our data is insufficient to test their relationship. A previous study
259 proposed a model with randomly oriented particles to explain the μ_g for pyrophyllite
260 (Sakuma et al. 2020). Although this model seems to quantitatively explain the μ_g for brucite,
261 the modeled macroscopic friction coefficients were generally lower than reported μ_g
262 (Figure 7). In the case of deformed gouges of layered structure minerals, alignment of the
263 platy particles has often been observed along localized shear bands such as Riedel shear, P,
264 and Y foliations (Moore and Lockner 2004; Haines et al. 2013) and the interactions at the

edges of aligned particles increases μ_g compared with μ_M (den Hartog et al. 2020). Some studies that used the foliated wafers of intact fault rocks reported clear differences in the friction coefficients from powdered fault rocks, which emphasizes the strong influence of fault fabric on frictional strengths (Collettini et al. 2009; Ikari et al. 2011). In future studies, such detailed microstructural information from experiments should be included in the model to account for the gouge frictional properties. These considerations of the frictional strength of gouge will be beneficial for modelling fault slip behavior and influence on earthquakes based on mineral compositions of the fault.

Conclusions

In this study, we theoretically calculated the atomic-scale interlayer frictional characteristics of gibbsite using the first-principles method based on density functional theory. The atomic-scale frictional characteristics were obtained using variations in the potential energy during interlayer deformation (PES), which are primarily controlled by stacking of hydroxyls on the octahedral sheets. The atomic-scale shear stress was calculated using the spatial derivative of PES. The high potential energy ridge in PES for gibbsite elongated parallel to [1 0 0] caused the shear direction dependence of the high and low

282 atomic-scale shear stresses observed subparallel to [0 1 0] and [1 0 0], respectively. Some
283 hydroxyls on gibbsite stand parallel to the layer and keep a distance from each other owing
284 to the existence of vacant sites within the octahedral sheet of gibbsite, leading to smaller
285 atomic-scale shear stress for gibbsite compared with brucite. The macroscopic interlayer
286 friction coefficient μ_M was calculated by the adhesion theory of friction using the obtained
287 interlayer atomic-scale frictional characteristics. The estimated μ_M for gibbsite based on the
288 atomic-scale interlayer shear stress $\tau_{atom}(p)$ of 0.65(9) for the reported yield strength p of
289 1.8(2) GPa is 0.36(6), which is clearly lower than the experimental friction coefficient μ_g of
290 0.74 for the dry powdered sample. This difference between μ_M and μ_g was also reported in
291 previous studies on layered structure minerals, suggesting the presence of additional
292 deformation mechanisms such as microstructures within the fault gouge that would be
293 useful for the practical estimation of fault slip behavior.
294

295 **Acknowledgement**

296 We thank Diane Moore and an anonymous reviewer for helpful comments. We also thank
297 Christopher J. Spiers for the constructive discussion. Computational resources were
298 provided by the “Initiative on Promotion of Supercomputing for Young or Women

299 Researchers" of the Supercomputing Division, Information Technology Center, University
300 of Tokyo and the "Joint Usage/Research Center for Interdisciplinary Large-scale
301 Information Infrastructures" in Japan (Project ID: EX18303). This study was partially
302 supported by KAKENHI JP20J20413. All crystal structures were drawn by VESTA
303 (Momma and Izumi 2011).

304

305 **References**

306 Behnsen, J., and Faulkner, D.R. (2012) The effect of mineralogy and effective normal stress on frictional
307 strength of sheet silicates. Journal of Structural Geology, 42, 49–61.
308 Bowden, F.P., and Tabor, D. (1950) The friction and lubrication of solids. Oxford University Press.
309 Byerlee, J.D. (1978) Friction of rocks. Pure and Applied Geophysics PAGEOPH, 116, 615–626.
310 Carpenter, B.M., Marone, C., and Saffer, D.M. (2011) Weakness of the San Andreas Fault revealed by
311 samples from the active fault zone. Nature Geoscience, 4, 251–254.
312 Collettini, C., Niemeijer, A.R., Viti, C., and Marone, C. (2009) Fault zone fabric and fault weakness. Nature,
313 462, 907–910.
314 Collettini, C., Tesei, T., Scuderi, M.M., Carpenter, B.M., and Viti, C. (2019) Beyond Byerlee friction, weak
315 faults and implications for slip behavior. Earth and Planetary Science Letters, 519, 245–263.

316 den Hartog, S.A.M., Faulkner, D.R., and Spiers, C.J. (2020) Low Friction Coefficient of Phyllosilicate Fault
317 Gouges and the Effect of Humidity: Insights From a New Microphysical Model. Journal of Geophysical
318 Research: Solid Earth, 125, e2019JB018683.
319 Garrity, K.F., Bennett, J.W., Rabe, K.M., and Vanderbilt, D. (2014) Pseudopotentials for high-throughput
320 DFT calculations. Computational Materials Science, 81, 446–452.
321 Giannozzi, P., Baroni, S., Bonini, N., Calandra, M., Car, R., Cavazzoni, C., Ceresoli, D., Chiarotti, G.L.,
322 Cococcioni, M., Dabo, I., and others (2009) QUANTUM ESPRESSO: a modular and open-source
323 software project for quantum simulations of materials. Journal of Physics: Condensed Matter, 21,
324 395502.
325 Grimme, S. (2006) Semiempirical GGA-type density functional constructed with a long-range dispersion
326 correction. Journal of Computational Chemistry, 27, 1787–1799.
327 Haines, S.H., Kaproth, B., Marone, C., Saffer, D.M., and van der Pluijm, B.A. (2013) Shear zones in clay-rich
328 fault gouge: A laboratory study of fabric development and evolution. Journal of Structural Geology, 51,
329 206–225.
330 Ikari, M.J., Niemeijer, A.R., and Marone, C. (2011) The role of fault zone fabric and lithification state on
331 frictional strength, constitutive behavior, and deformation microstructure. Journal of Geophysical
332 Research: Solid Earth, 116, 1–25.

Ikari, M.J., Kopf, A.J., Hüpers, A., and Vogt, C. (2018) Lithologic control of frictional strength variations in subduction zone sediment inputs. Geosphere, 14, 604–625.

Kawai, K., Sakuma, H., Katayama, I., and Tamura, K. (2015) Frictional characteristics of single and polycrystalline muscovite and influence of fluid chemistry. Journal of Geophysical Research: Solid Earth, 120, 6209–6218.

Lockner, D.A., Morrow, C.A., Moore, D.E., and Hickman, S.H. (2011) Low strength of deep San Andreas fault gouge from SAFOD core. Nature, 472, 82–85.

Momma, K., and Izumi, F. (2011) VESTA 3 for three-dimensional visualization of crystal, volumetric and morphology data. Journal of Applied Crystallography, 44, 1272–1276.

Monkhorst, H.J., and Pack, J.D. (1976) Special points for Brillouin-zone integrations. Physical Review B, 13, 5188–5192.

Moore, D.E., and Lockner, D.A. (2004) Crystallographic controls on the frictional behavior of dry and water-saturated sheet structure minerals. Journal of Geophysical Research, 109, B03401.

Morrow, C.A., Moore, D.E., and Lockner, D.A. (2000) The effect of mineral bond strength and adsorbed water on fault gouge frictional strength. Geophysical Research Letters, 27, 815–818.

Niemeijer, A.R. (2018) Velocity-dependent slip weakening by the combined operation of pressure solution and foliation development. Scientific Reports, 8, 4724.

Okamoto, A.S., Verberne, B.A., Niemeijer, A.R., Takahashi, M., Shimizu, I., Ueda, T., and Spiers, C.J. (2019) Frictional Properties of Simulated Chlorite Gouge at Hydrothermal Conditions: Implications for Subduction Megathrusts. Journal of Geophysical Research: Solid Earth, 124, 4545–4565.

Okuda, H., Kawai, K., and Sakuma, H. (2019) First-principles Investigation of Frictional Characteristics of Brucite: An Application to Its Macroscopic Frictional Characteristics. Journal of Geophysical Research: Solid Earth, 124, 10423–10443.

Okuda, H., Katayama, I., Sakuma, H., and Kawai, K. (2021a) Effect of normal stress on the frictional behavior of brucite: application to slow earthquakes at the subduction plate interface in the mantle wedge. Solid Earth, 12, 171–186.

Okuda, H., Ikari, M.J., Roesner, A., Stanislowski, K., Hüpers, A., Yamaguchi, A., and Kopf, A.J. (2021b) Spatial Patterns in Frictional Behavior of Sediments Along the Kumano Transect in the Nankai Trough. Journal of Geophysical Research: Solid Earth, 126.

Perdew, J.P., Burke, K., and Ernzerhof, M. (1996) Generalized Gradient Approximation Made Simple. Physical Review Letters, 77, 3865–3868.

Saalfeld, H., and Wedde, M. (1974) Refinement of the crystal structure of gibbsite, Al(OH) 3. Zeitschrift für Kristallographie, 139, 129–135.

Sakuma, H., and Suehara, S. (2015) Interlayer bonding energy of layered minerals: Implication for the

relationship with friction coefficient. Journal of Geophysical Research: Solid Earth, 120, 2212–2219.

Sakuma, H., Kawai, K., Katayama, I., and Suehara, S. (2018) What is the origin of macroscopic friction? Science Advances, 4, eaav2268.

Sakuma, H., Kawai, K., and Kogure, T. (2020) Interlayer energy of pyrophyllite: Implications for macroscopic friction. American Mineralogist, 105, 1204–1211.

Sakuma, H., Lockner, D.A., Solum, J., and Davatzes, N.C. (2022) Friction in clay-bearing faults increases with the ionic radius of interlayer cations. Communications Earth & Environment, 3, 116.

Tománek, D., Zhong, W., and Thomas, H. (1991) Calculation of an Atomically Modulated Friction Force in Atomic-Force Microscopy. Europhysics Letters (EPL), 15, 887–892.

Viti, C., and Collettini, C. (2009) Growth and deformation mechanisms of talc along a natural fault: a micro/nanostructural investigation. Contributions to Mineralogy and Petrology, 158, 529–542.

Wijayaratne, H., McIntosh, G., Hyland, M., Perander, L., and Metson, J. (2017) Relationships Between Smelter Grade Alumina Characteristics and Strength Determined by Nanoindentation and Ultrasound-Mediated Particle Breakage. Metallurgical and Materials Transactions A, 48, 3046–3059.

Zhong, W., and Tománek, D. (1990) First-principles theory of atomic-scale friction. Physical Review Letters, 64, 3054–3057.

384

385 **Table 1.** Interlayer friction coefficients for layered structure minerals. $\tau_{ave}(p)$: Theoretically
386 calculated atomic-scale interlayer friction τ_{ave} under the normal stress of p (yield strength of
387 the material); μ_M: Interlayer macroscopic friction coefficient calculated as $\tau_{ave}(p)/p$
388 (equation 7); μ_g: Experimentally obtained gouge friction coefficients.

Mineral	$\tau_{ave}(p)$ (GPa)	p (GPa)	μ_M	μ_g
Gibbsite	0.65(9)[a]	1.8(2)[b]	0.36(6)[a]	0.74[c]
Brucite	1.23(6)[d]	4.03(36)[d]	0.31(3)[d]	0.39[e]
Muscovite	1.40(31)[f]	6.27(26)[f]	0.22(5)[f]	0.50[g]
Pyrophyllite	0.44(7)[h]	3.3(4)[i]	0.13(3)[h]	0.38[c]

[a]This study. [b]Wijayaratne et al. (2017). [c]Moore and Lockner (2004). The error for brucite represents the range of stick-slip behavior. [d]Okuda et al. (2019). [e]Okuda et al. (2021a). [f]Sakuma et al. (2018). [g]Kawai et al. (2015). [h]Sakuma et al. (2020). [i]Zhang et al. (2013).

389

390

391

Figure 1.

Crystal structures of (**a**) gibbsite and (**b**) brucite. The layers in the upper panels are the lowest layer of each material. The areas surrounded by black lines are the primitive unit cells for gibbsite and brucite.

Figure 2

(**a**) Configuration of the supercell for gibbsite used in this study. The shaded area represents the basal area S of the supercell. The shear plane is located between two layers of gibbsite. A three-dimensional periodic boundary condition was employed, and sufficient vacuum space (>20 Å normal to the layers) was used to avoid artificial effects due to the periodic boundary condition (**b**) Relationship between interlayer displacement z from the most stable interlayer distance of 4.750 Å, and potential energy E_{ad}. The inset shows the relationship between z and the normal stress σ_n calculated using equation 3. The lines show the data at the positions of top layer at (e) (solid black line with black circles), (j) (grey line with white circles), and (f) (black dashed line with black triangles) in Figure 4c.

Figure 3.

409 Schematic illustration of the relation between (**a**) potential energy and (**b**) shear force
410 during the relative deformation of the top and bottom layers (illustrated at the top) under a
411 constant normal force. The total of potential increase ΔPE_i during each conservative parts
412 of sliding directly contributes to the atomic-scale shear force (equation 5).
413
414 **Figure 4.**
415 PESs for gibbsite (**a** and **c**) and brucite (**b** and **d**) under normal stresses of 0.0 GPa and 5.0
416 GPa, respectively. The areas surrounded by white lines represent the basal area of the
417 primitive unit cell for each material (a = 8.673 Å, b =5.054 Å for gibbsite; a = 3.1453 Å for
418 brucite (Okuda et al. 2019)). The most stable and unstable crystal structures are displayed
419 in (**e**)-(**h**), corresponding to the displacement of top layer indicated by X marks in (**c**) and
420 (**d**). At stable stackings, the hydroxyls on the upper and lower layers do not face each other
421 (**e** and **g**), whereas some hydroxyls face each other, as indicated by black circles, at unstable
422 stackings (**f** and **h**). Data for the PESs of brucite (**b** and **d**) are from Okuda et al. (2019). (**i**
423 and **j**) Crystal structures at the position of top layer at (i) and (j) in (**c**). Some hydroxyls (in
424 this case, H8, H9, H12, H13, H16, and H17) change their angles during deformation.
425

426 **Figure 5.**

427 (**a**) Normal stress dependence of the atomic-scale shear stress τ_{ave} for gibbsite (black line)
428 and brucite (gray line). The error bars represent the standard deviation of 360 linear sliding
429 paths. (**b**) Shear stresses at a normal stress of 2.5 GPa of 360 linear sliding paths for
430 gibbsite (black) and brucite (gray).

431

432 **Figure 6.**

433 (**a**) PES for gibbsite at a normal stress of 2.5 GPa. Paths [2 1 0] and [1 3 0] are indicated.
434 The circles are the locations corresponding to the area of the highest potential energy. (**b**)
435 Potential energy profiles at a normal stress of 2.5 GPa along paths [2 1 0] (black) and [1 3
436 0] (gray). Cumulative potential energies during the conservative part of sliding (**c**) and
437 shear stresses (**d**) for the two paths at a normal stress of 2.5 GPa. The dotted lines in (**d**) are
438 the shear stresses during the nonconservative part of sliding. The gray hatched areas show
439 the regions where higher shear stresses are required to climb the highest potential energy
440 indicated by circles in (**a**).

441

442 **Figure 7.**

443 Relation between the gouge friction coefficient μ_g and the interlayer friction coefficient μ_M.

444 Black solid line represents the case when μ_M and μ_g are identical. Gray solid curve

445 represents the model assuming a random orientation of the gouge particles (Sakuma et al.

446 2020; see Table 1 for references).

447

448

This is the peer-reviewed, final accepted version for American Mineralogist, published by the Mineralogical Society of America.
The published version is subject to change. Cite as Authors (Year) Title. American Mineralogist, in press.
DOI: https://doi.org/10.2138/am-2022-8561. http://www.minsocam.org/

Figure 1

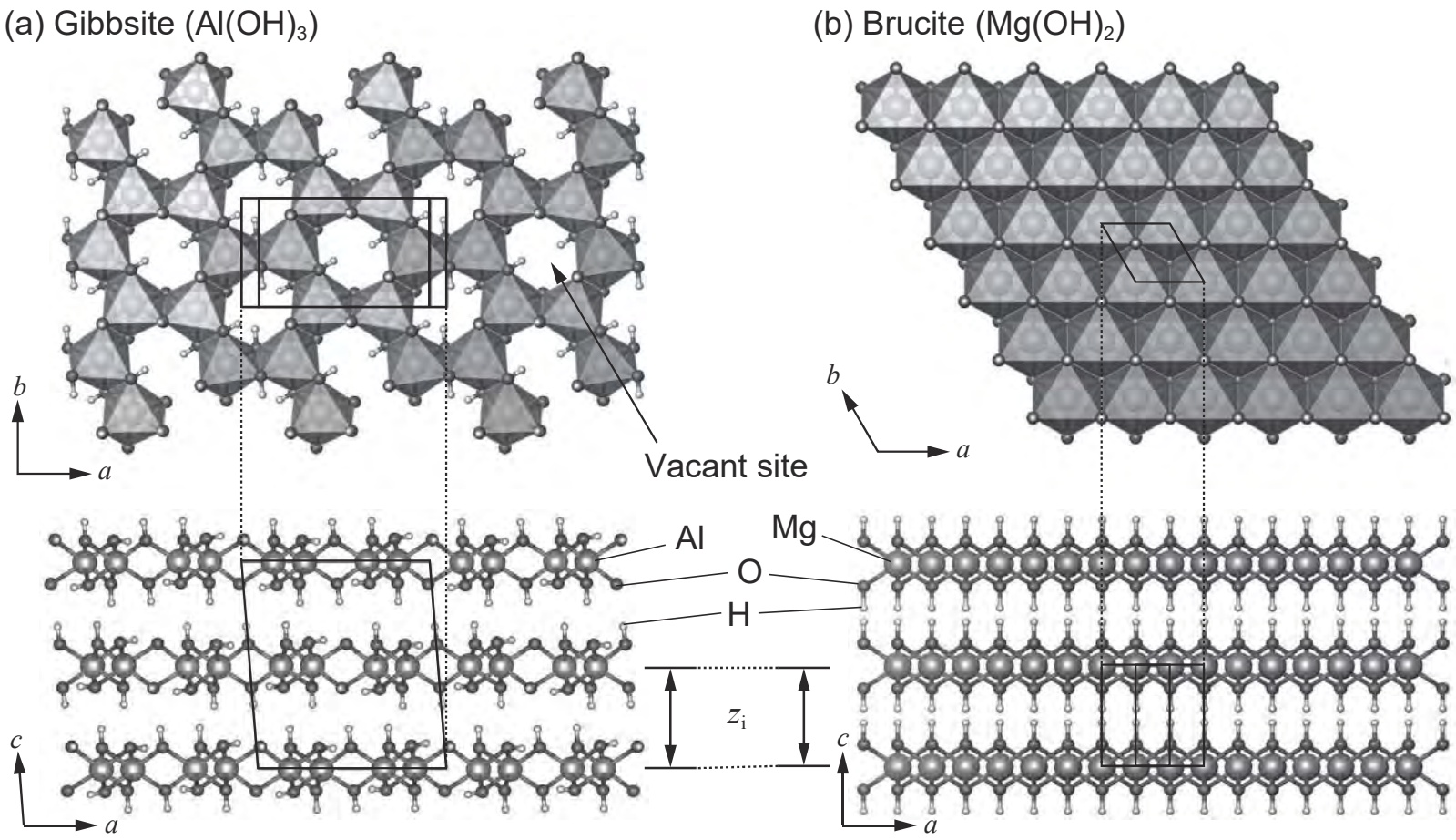

This is the peer-reviewed, final accepted version for American Mineralogist, published by the Mineralogical Society of America.
The published version is subject to change. Cite as Authors (Year) Title. American Mineralogist, in press.
DOI: https://doi.org/10.2138/am-2022-8561. http://www.minsocam.org/

Figure 2

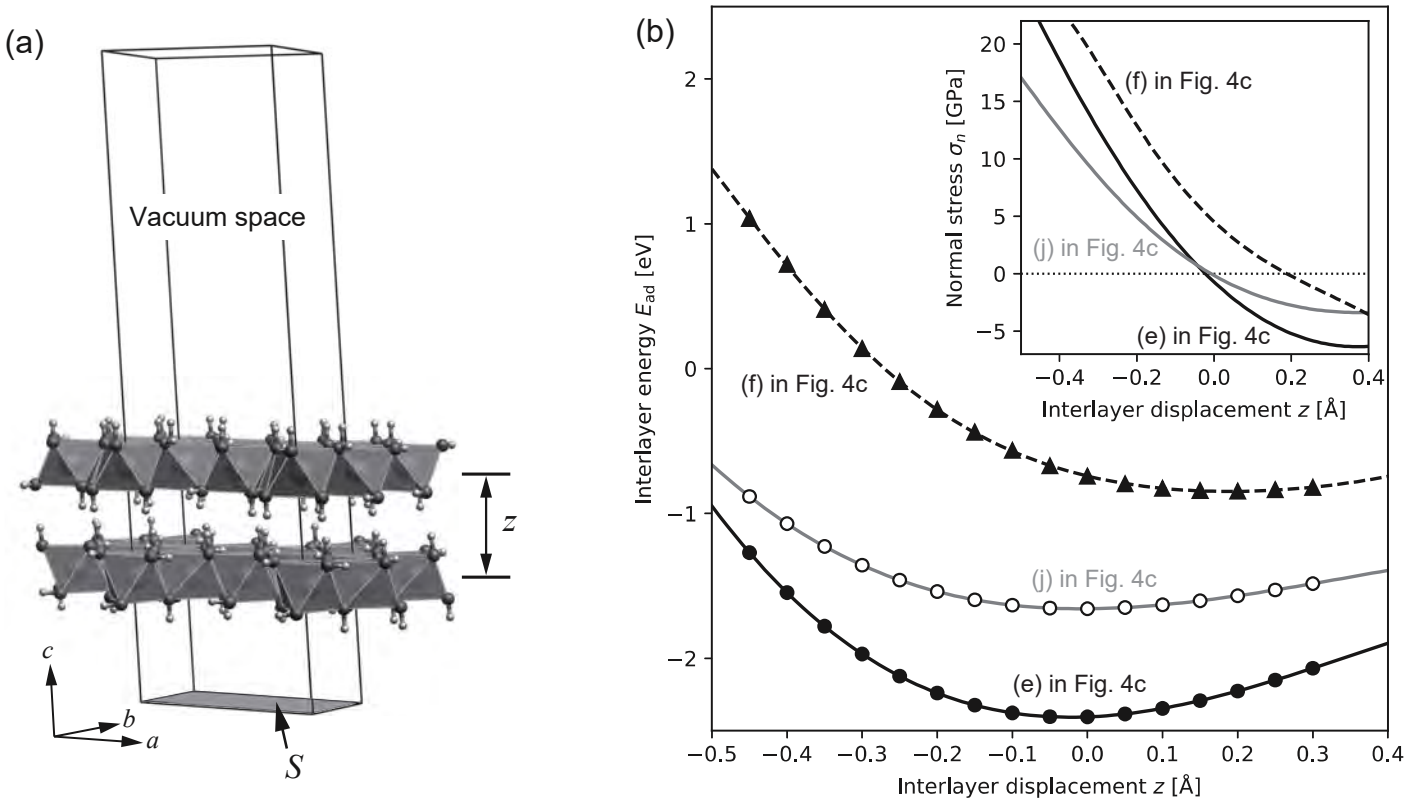

This is the peer-reviewed, final accepted version for American Mineralogist, published by the Mineralogical Society of America.
The published version is subject to change. Cite as Authors (Year) Title. American Mineralogist, in press.
DOI: https://doi.org/10.2138/am-2022-8561. http://www.minsocam.org/

Figure 3

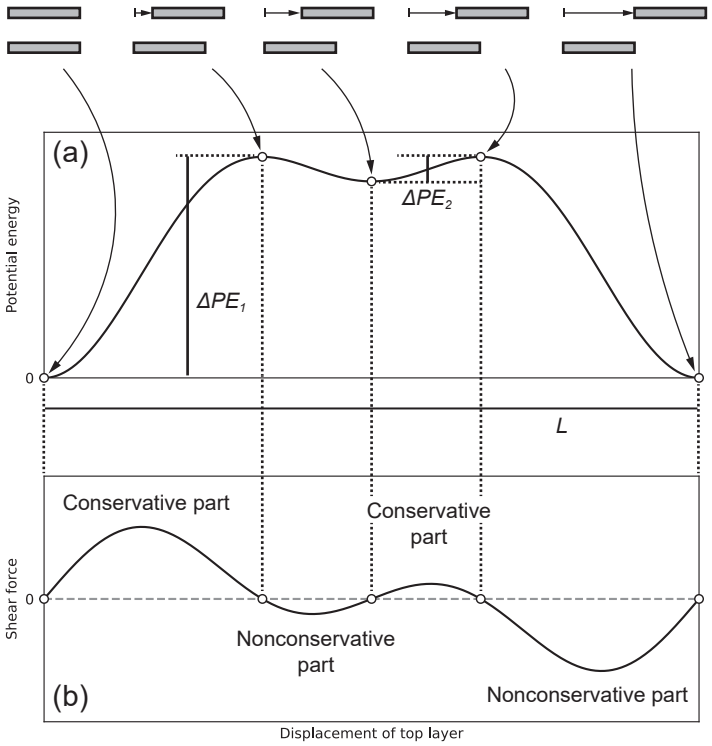

This is the peer-reviewed, final accepted version for American Mineralogist, published by the Mineralogical Society of America.
The published version is subject to change. Cite as Authors (Year) Title. American Mineralogist, in press.
DOI: https://doi.org/10.2138/am-2022-8561. http://www.minsocam.org/

Figure 4

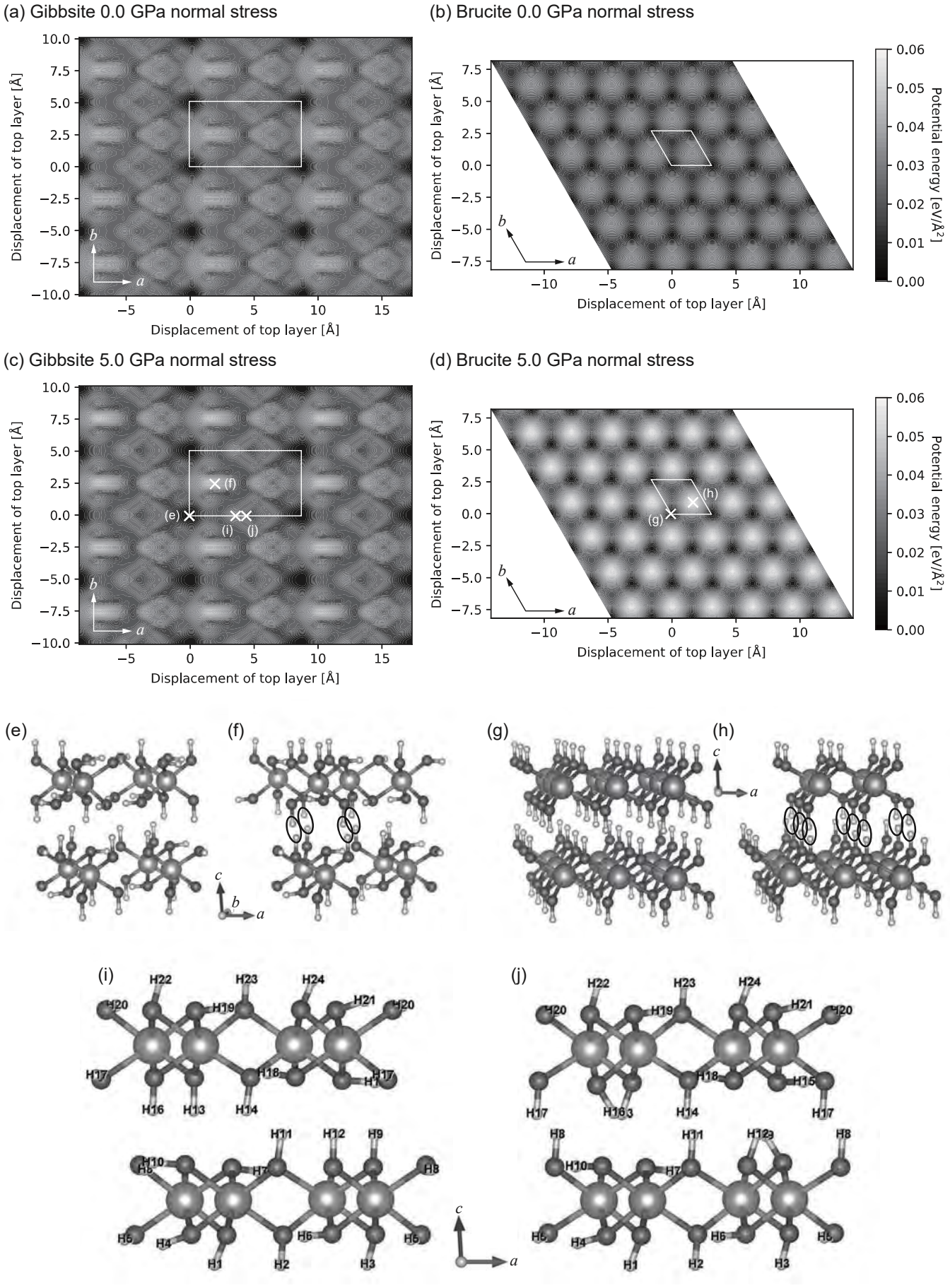

This is the peer-reviewed, final accepted version for American Mineralogist, published by the Mineralogical Society of America.
The published version is subject to change. Cite as Authors (Year) Title. American Mineralogist, in press.
DOI: https://doi.org/10.2138/am-2022-8561. http://www.minsocam.org/

Figure 5

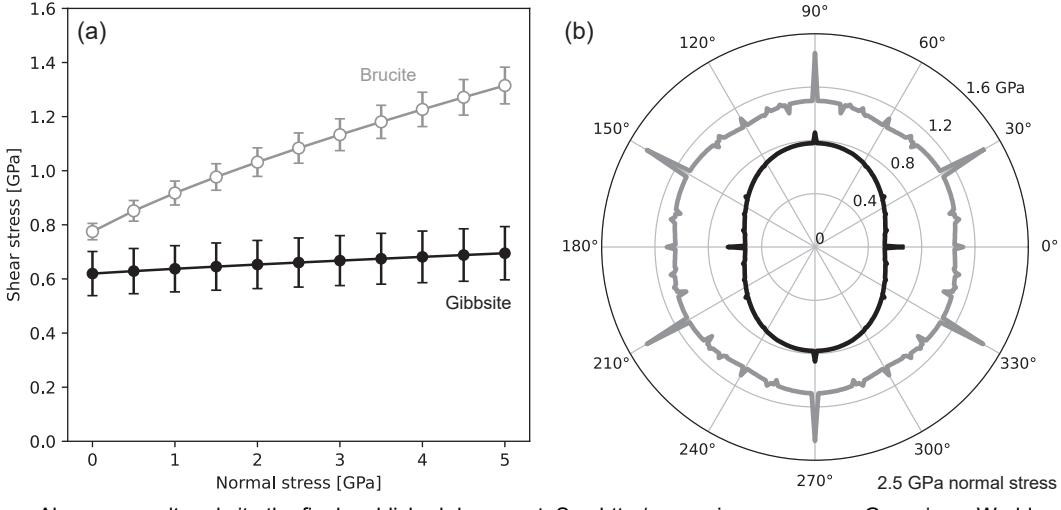

This is the peer-reviewed, final accepted version for American Mineralogist, published by the Mineralogical Society of America.
The published version is subject to change. Cite as Authors (Year) Title. American Mineralogist, in press.
DOI: https://doi.org/10.2138/am-2022-8561. http://www.minsocam.org/

Figure 6

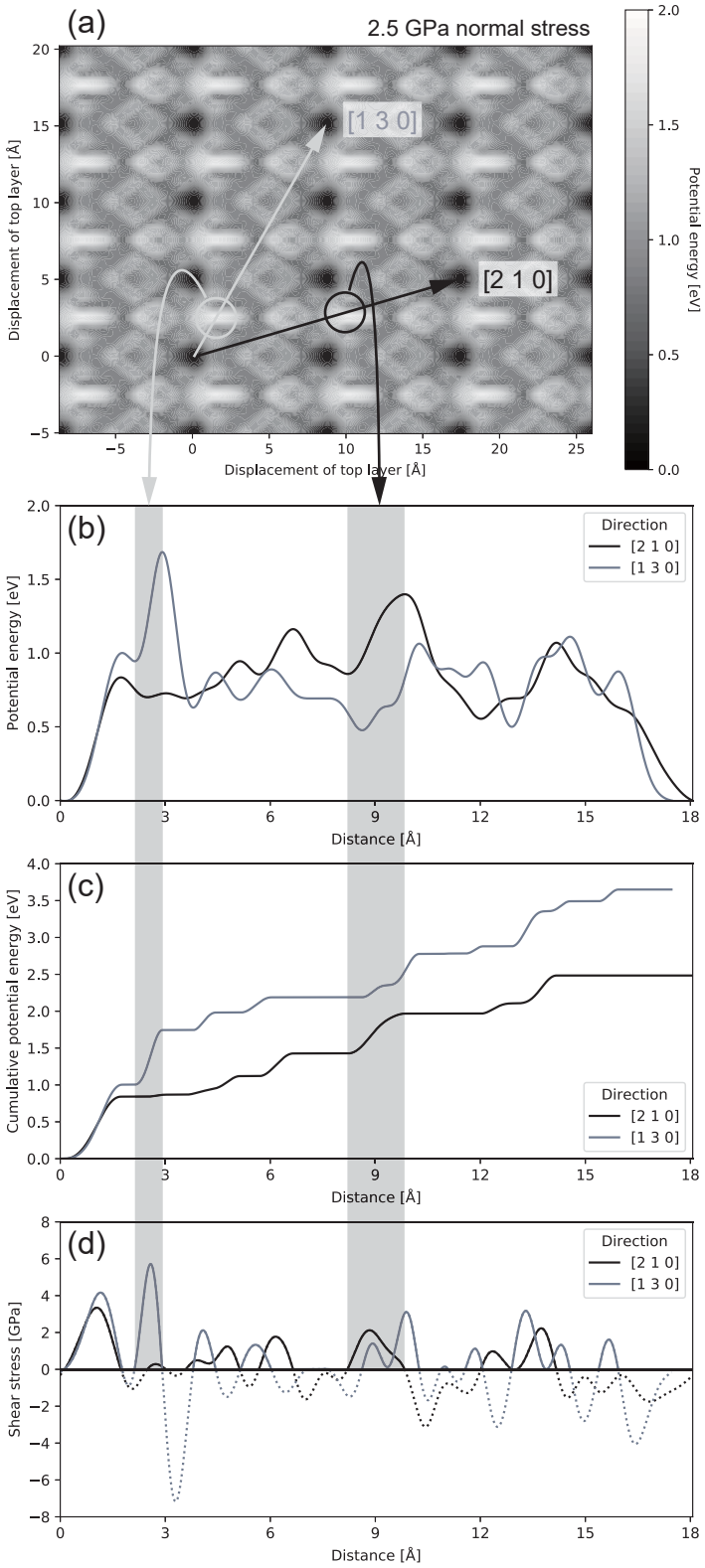

This is the peer-reviewed, final accepted version for American Mineralogist, published by the Mineralogical Society of America.
The published version is subject to change. Cite as Authors (Year) Title. American Mineralogist, in press.
DOI: https://doi.org/10.2138/am-2022-8561. http://www.minsocam.org/

Figure 7